scientific reports

Check for updates

OPEN

Deficiency of the lipid flippase ATP10A causes diet-induced dyslipidemia in female mice

Adriana C. Norris[1], Eugenia M. Yazlovitskaya[1], Lin Zhu[2], Bailey S. Rose[3,4,5,6,7], Jody C. May[3,4,5,6,7], Katherine N. Gibson-Corley[8], John A. McLean[3,4,5,6,7], John M. Stafford[2,9,10] & Todd R. Graham[1]✉

Genetic association studies have linked ATP10A and closely related type IV P-type ATPases (P4-ATPases) to insulin resistance and vascular complications, such as atherosclerosis. ATP10A translocates phosphatidylcholine and glucosylceramide across cell membranes, and these lipids or their metabolites play important roles in signal transduction pathways regulating metabolism. However, the influence of ATP10A on lipid metabolism in mice has not been explored. Here, we generated gene-specific *Atp10A* knockout mice and show that *Atp10A*$^{-/-}$ mice fed a high-fat diet did not gain excess weight relative to wild-type littermates. However, *Atp10A*$^{-/-}$ mice displayed female-specific dyslipidemia characterized by elevated plasma triglycerides, free fatty acids and cholesterol, as well as altered VLDL and HDL properties. We also observed increased circulating levels of several sphingolipid species along with reduced levels of eicosanoids and bile acids. The *Atp10A*$^{-/-}$ mice also displayed hepatic insulin resistance without perturbations to whole-body glucose homeostasis. Thus, ATP10A has a sex-specific role in regulating plasma lipid composition and maintaining hepatic liver insulin sensitivity in mice.

The metabolic syndrome is a complex condition that affects 33% of Americans[1] and on a global scale, over 1 billion people[2]. This syndrome is characterized by abdominal obesity, insulin resistance, hypertension, and dyslipidemia, and an increased risk of developing type 2 diabetes mellitus and atherosclerotic cardiovascular disease (ASCVD)[3]. Commonly found variants in *ATP10A* have been linked to increased risk of insulin resistance[4] and variants within a related gene, *ATP10D*, have been linked to increased atherosclerosis risk[5]. ATP10A and ATP10D are P4-ATPases, also known as lipid flippases, that translocate lipids from the exoplasmic or luminal leaflets to cytosolic leaflets of cell membranes. This creates an asymmetric distribution of lipids within membranes that has several implications for the cell[6], including in apoptosis[7], vesicular trafficking[8], and signal transduction[9].

Interestingly, most of the 14 human P4-ATPases have established roles in disease, such as in severe neurological disorders and intrahepatic cholestasis[10]. These enzymes transport specific lipid substrates, which are closely related to their cellular and physiological functions. ATP10A flips phosphatidylcholine (PC)[11] and glucosylceramide (GlcCer)[12]. PC is the most abundant phospholipid in cellular membranes[13]. Metabolites of PC, such as lysophosphatidylcholine (LysoPC), arachidonic acid (AA), and eicosanoids produced from AA, play important roles in modulating inflammation and various disease states[14–18]. GlcCer is a bioactive lipid that can affect insulin signaling and energy homeostasis[19], as well as inflammation[20]. Inhibiting GlcCer synthase enhances insulin sensitivity[21] and protects against cardiac hypertrophy[22]. GlcCer can be broken down into ceramide or built up into gangliosides, which also have established roles in metabolism[23–25].

Previous reports suggested a role for murine ATP10A in diet-induced obesity, insulin resistance, and dyslipidemia and these phenotypes were more severe in female mice[26,27]. However, the mouse model used in these studies contained a large, irradiation-induced chromosomal deletion ($p^{23DFiOD}$) encompassing the pink-eyed

[1]Department of Biological Sciences, Vanderbilt University, 465 21St Ave S, Nashville, TN 37212, USA. [2]Division of Endocrinology, Diabetes and Metabolism, Vanderbilt University Medical Center, Nashville, TN, USA. [3]Department of Chemistry, Vanderbilt University, Nashville, TN, USA. [4]Center for Innovative Technology, Vanderbilt University, Nashville, TN, USA. [5]Vanderbilt-Ingram Cancer Center, Vanderbilt University, Nashville, TN, USA. [6]Vanderbilt Institute of Chemical Biology, Vanderbilt University, Nashville, TN, USA. [7]Vanderbilt Institute for Integrative Biosystems Research and Education, Vanderbilt University, Nashville, TN, USA. [8]Division of Comparative Medicine, Department of Pathology, Microbiology and Immunology, Vanderbilt University Medical Center, Nashville, TN, USA. [9]Tennessee Valley Healthcare System, Veterans Affairs, Nashville, TN, USA. [10]Department of Molecular Physiology and Biophysics, Vanderbilt University, Nashville, TN, USA. ✉email: tr.graham@vanderbilt.edu

dilution (*p)* locus, *Atp10A* (previously named *Atp10C)* and several other genes. End-point mapping of a nested deletion series implicated *Atp10A* in the metabolic defects but whether an *Atp10A*-specific knockout is sufficient to cause insulin resistance has not been determined. Homozygosity of the irradiation-induced deletion resulted in embryonic lethality and heterozygous mice that inherited the chromosomal deletion maternally displayed more severe metabolic phenotypes compared to those who inherited the deletion paternally. This observation suggested that the *Atp10A* locus was imprinted to suppress expression of the paternal allele, however several studies failed to detect imprinted expression of the *ATP10A* gene[28–30]. It appears that *ATP10A* expression pattern is complex and dependent on multiple factors including gender, genetic background, and tissue type.

Although correlations between *ATP10A* deficiency and insulin resistance, diet-induced obesity, and glucose uptake[31] have been reported, it is unclear whether this flippase plays a causative role in these processes. Here, we generated a gene-specific deletion and tested the impact of *Atp10A* deficiency in mice during high fat diet (HFD) feeding. *Atp10A* deficient mice display female-specific diet-induced dyslipidemia, broad changes to lipid metabolism, and disruptions in liver insulin signaling.

Results

Atp10A deficiency does not affect body composition after high fat diet feeding

To develop the $Atp10A^{-/-}$ mice, we created a gene-specific knockout allele of *Atp10A* in the C57BL/6J background using CRISPR/Cas9 guide RNA sequences targeted to regions flanking exon 2 (Fig. 1a) and verified the genotype of the mice via PCR analysis (Fig. 1b) and subsequent sequencing of the PCR products corresponding to the WT and KO bands (Fig. 1c, Supplemental Fig. 1). To test the potential impact of *Atp10A* on weight gain, we placed male and female WT ($10A^{+/+}$) and KO ($10A^{-/-}$) mice on a HFD for 12 weeks. We found that there was no significant difference in weight gain in males (*P*-value for 12th week on HFD: 0.3154) or females (*P*-value for 12th week on HFD: > 0.9999) based on genotype (Fig. 1d). We next examined body composition and size and found that male and female mice did not display a difference in % lean mass (Fig. 1e) or % fat mass (Fig. 1f) based on genotype. Male mice also did not exhibit changes in body length based on genotype, however, female $Atp10A^{-/-}$ mice had shorter body lengths compared to $Atp10A^{+/+}$ littermates (Fig. 1g). For the female mice, no significant difference was observed in daily (sum of light and dark hours) activity, food intake, or energy expenditure based on genotype. However, the $Atp10A^{-/-}$ female mice displayed reduced food intake and a negative energy balance during light hours compared to WT mice (Supplemental table 1). Additionally, we did not observe any changes in tissue mass (Fig. 1h) in female mice based on genotype. We also measured weight gain, body composition, and body length in female mice on normal chow; and found no significant differences based on genotype (Supplemental Fig. 2a–d). Altogether, these results indicate that *Atp10A* deficiency does not alter the development of diet-induced obesity under the conditions tested.

Atp10A deficiency does not affect whole-body glucose homeostasis in female mice

Studies using the $p^{23DFiOD}$ deletion encompassing *Atp10A,* found that these mice were hyperinsulinemic, insulin resistant, and hyperglycemic[26,27]. To specifically assess the influence of *Atp10A* on glucose homeostasis, we fasted WT and $Atp10A^{-/-}$ (exon 2 deletion) mice for 5 h and performed an oral glucose tolerance test (OGTT) as well as measured fasting levels of glucose and insulin. During the OGTT, male *Atp10A* deficient mice trended towards an increased glucose excursion after the glucose bolus (Fig. 2a), but this was not significant when compared to WT mice. The female $Atp10A^{-/-}$ mice exhibited significantly elevated fasting blood glucose after a 5 h fast (points before time 0 during the OGTT, Fig. 2b) and trended toward exhibiting an elevated glucose excursion compared to the female WT mice, represented by the elevated area under the curve (AUC) (Fig. 2b, inset). While the elevated fasting blood glucose was significant for the number of female mutant mice tested (n = 6), the study was underpowered. Therefore, fasting blood glucose was measured from additional mice and we found no significant difference in fasting blood glucose in male or female mice based on genotype (Fig. 2c). The underlying cause of the variation in fasting blood glucose levels observed in female mice remains uncertain, as all mice received uniform treatment. This variability may stem from factors such as individual differences in food consumption, the time between the last meal and sacrifice, social dynamics within the cage, or other potential variables. Nevertheless, it's worth noting that the observed variance falls within the expected range of glucose levels in animals. There was also no significant difference in fasting plasma insulin (Fig. 2d) or insulin levels at 30 min (T30, Fig. 2e), or 60 min (T60, Fig. 2f) after the glucose bolus (during the OGTT) in males or females based on genotype. Additionally, normal chow fed female $Atp10A^{-/-}$ mice did not exhibit differences in fasting blood glucose or insulin (Supplemental Fig. 2e,f) compared to WT mice. Therefore, in contrast to expectations based on prior reports, *Atp10A* deficiency does not appear to significantly perturb whole-body glucose homeostasis.

Maternal inheritance of the *Atp10A* exon 2 deletion results in changes to body length and fasting blood glucose in males

Prior reports showed that the inheritance pattern of the $p^{23DFiOD}$ deletion encompassing *Atp10A* effected the severity of the metabolic phenotypes in heterozygous mice, specifically if the deletion was inherited maternally or paternally[26,27]. We tested this phenomenon using the *Atp10A* exon 2 deletion mice by measuring metabolic phenotypes after high fat diet feeding, in heterozygous mice reared from $10A^{+/-}$ dams x $10A^{+/+}$ sires (maternal inheritance (inh.)) or $10A^{+/+}$ dams x $10A^{+/-}$ sires (paternal inh.). We found no significant difference in weight gain, body composition, or fasting plasma insulin based on the inheritance patterns of the *Atp10A* exon 2 deletion in males or females after 12 weeks of HFD (Supplemental Fig. 3a–c,f). However, the male mice inheriting the exon 2 deletion maternally trended toward having increased weight gain, although this did not reach statistical significance (P-value for 12^{th} week of HFD: 0.0906), shorter bodies (Supplemental Fig. 3d) and elevated fasting blood glucose levels after a 5 h fast (Supplemental Fig. 3e) compared to mice that inherited the deletion paternally.

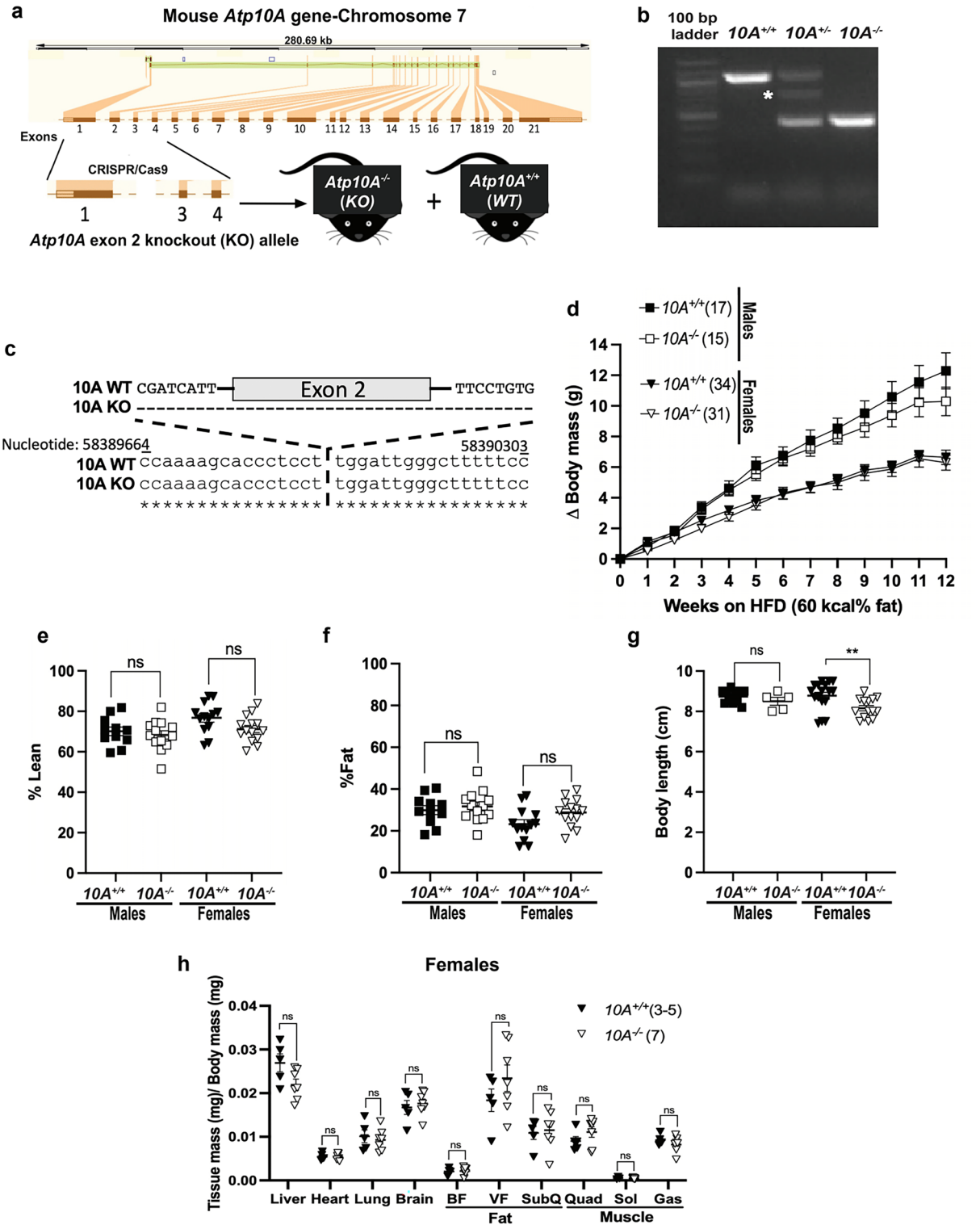

Figure 1. Atp10A deletion does not alter the development of diet-induced obesity after 12 weeks of HFD. (**a**) Graphic illustrating how CRISPR/cas9 was used to delete exon 2 in the mouse Atp10A to create the Atp10A$^{-/-}$ (KO) mouse line. (**b**) PCR genotyping results from Atp10A$^{+/+}$ (10A$^{+/+}$) (1067 base pairs (bp)), Atp10A$^{+/-}$ (10A$^{+/-}$), and Atp10A$^{-/-}$ (10A$^{-/-}$) (460 bp) mouse tail clips. The white asterisk indicates a product at ~ 700 bp that appears in all 10A$^{+/-}$ samples due to hybridization of sequences from the 10A$^{+/+}$ and 10A$^{-/-}$ PCR products. An uncropped image of the gel is shown in Supplemental Fig. 7A. (**c**) Sequence alignment of the PCR products from 10A$^{+/+}$ and 10A$^{-/-}$ mice (visualized in in Fig. 1b, Supplemental Fig. 1). The alignment was generated using EMBOSS Needle. (**d**) Weight gain of male and female 10A$^{+/+}$ and 10A$^{-/-}$ mice over the course of 12 weeks on a HFD (60 kcal% fat, Ad lib feeding) (**Male:** 10A$^{+/+}$ n = 17, 10A$^{-/-}$ n = 15; **Female:** 10A$^{+/+}$ n = 34, 10A$^{-/-}$ n = 31). (**e**) Lean and (**f**) fat body mass were normalized to the combined sum of lean and fat mass to calculate % Lean and % Fat mass (**Male**: 10A$^{+/+}$ n = 11,10A$^{-/-}$ n = 13; **Female**:10A$^{+/+}$ n = 13,10A$^{-/-}$ n = 14). (**g**) Body length of mice was measured after CO_2 sacrifice, **P = 0.0094. (**Male:** 10A$^{+/+}$ n = 11, 10A$^{-/-}$ n = 5; **Female**: 10A$^{+/+}$ n = 17, 10A$^{-/-}$ n = 14). (**h**) The wet mass of tissue was measured after removal from female mice on the 12th week on the HFD. Tissue mass is normalized to body mass (10A$^{+/+}$ n = 3–5,10A$^{-/-}$ n = 7). P value by (**d**) 2-way ANOVA with Sidak's multiple comparison or (**e**–**h**) unpaired t-tests.

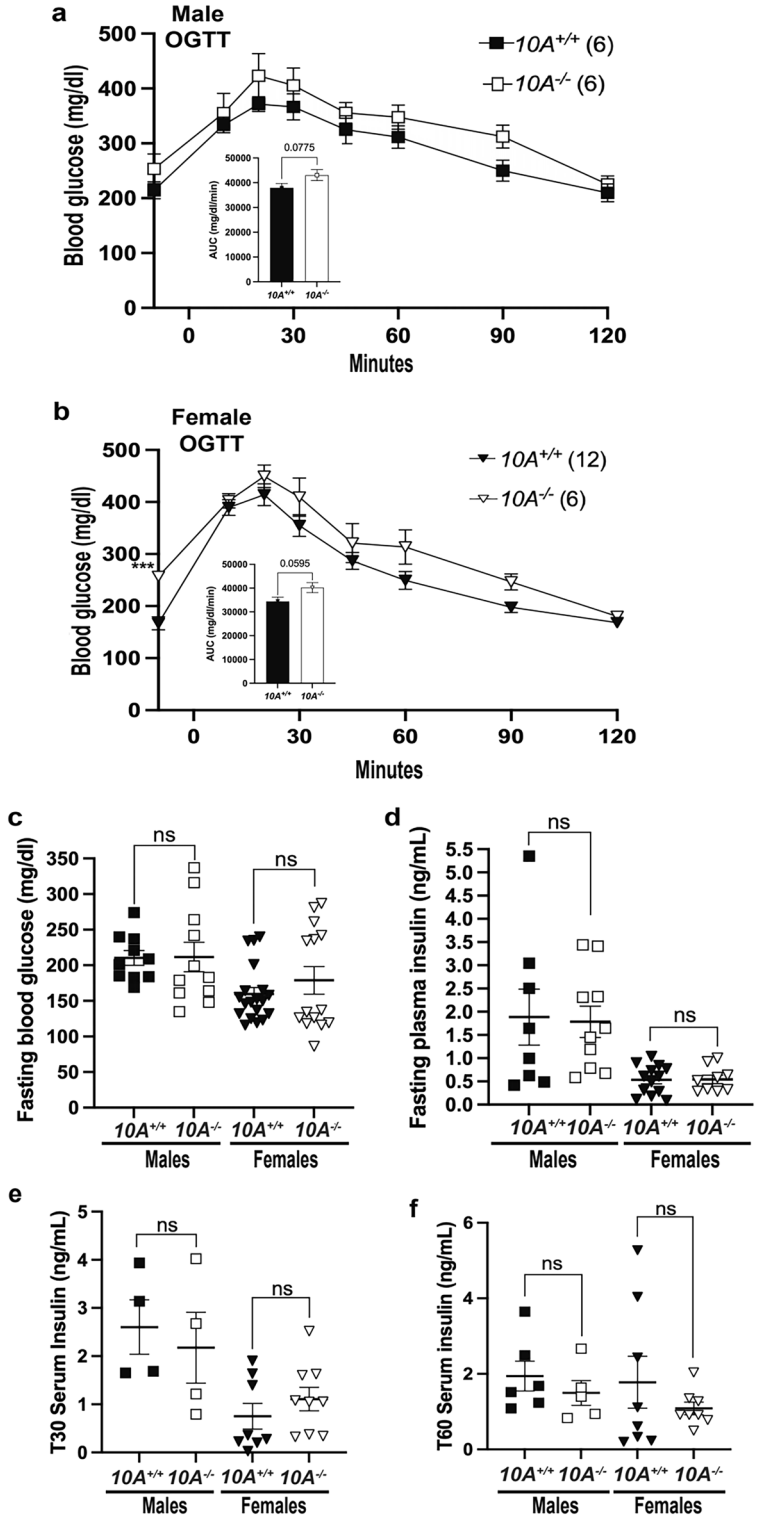

Figure 2. *Atp10A* deletion does not result in changes to glucose homeostasis after 12 weeks of HFD. (**a**) Male and (**b**) female mice were gavaged with 20% dextrose (time 0 on the graph) after a 5-h fast then an oral glucose tolerance test (OGTT) was performed. The inset shows the area under the curve (AUC) of the blood glucose (mg/dl) during the OGTT, normalized to fasting blood glucose (points before time 0 on the graph), ***$P = 0.0003$. **Male:** $10A^{+/+}$ n = 6,$10A^{-/-}$ n = 6; **Female**: $10A^{+/+}$ n = 12, $10A^{-/-}$ n = 6) (**c**) Fasting blood glucose was measured from tail blood after a 5 h fast, via a glucometer **(Male:** $10A^{+/+}$ n = 10, $10A^{-/-}$ n = 11; **Female**: $10A^{+/+}$ n = 19, $10A^{-/-}$ n = 14). (**d**) Fasting plasma insulin was measured after a 5 h fast (**Male:** $10A^{+/+}$ n = 8, $10A^{-/-}$ n = 10; **Female:** $10A^{+/+}$ n = 13,$10A^{-/-}$ n = 9). Insulin was measured from serum collected during the OGTT shown in Fig. 2a,b at the (**e**) 30-min time point (T30) and the (**f**) 60-min time point (T60), (**Male:** E: $10A^{+/+}$ n = 4, $10A^{-/-}$ n = 4, F: $10A^{+/+}$ n = 6, $10A^{-/-}$ n = 5; **Female**: $10A^{+/+}$ n = 8, $10A^{-/-}$ n = 6). P value by (**a**,**b**, not AUC) 2-way ANOVA with Sidak's multiple comparison or (**a**,**b** (AUC), **c**–**f**) unpaired t-tests.

Therefore, the inheritance pattern of the *Atp10A* exon 2 deletion does not significantly impact weight gain, body composition, and fasting plasma insulin in males or females after HFD feeding, but does have distinct effects on body length and fasting blood glucose levels in male mice.

Atp10A deficiency causes diet-induced dyslipidemia in females

To further probe the influence of *Atp10A* on whole-body metabolism, we measured the concentration of free fatty acids (FFA), cholesterol (chol), and triglycerides (TG) in the plasma. While the male mice showed no difference in plasma lipids based on genotype (Supplemental Fig. 4a–c), the female *Atp10A*$^{-/-}$ mice display substantially elevated plasma concentrations of FFA (Fig. 3a), chol (Fig. 3b), and TG (Fig. 3c) compared to *Atp10A*$^{+/+}$ littermates. To further explore this female-specific dyslipidemia phenotype, we performed fast performance liquid chromatography (FPLC) on plasma to assess the relative size and lipid distribution in lipoprotein fractions (Fig. 3d). We found that the *Atp10A*$^{-/-}$ mice carry most of their TG and cholesterol in smaller sized very low-density lipoprotein (VLDL) and high-density lipoprotein (HDL) particles, respectively (indicated by a shift to the right in the chromatograms). We also compared the AUC of the VLDL-TG (Fig. 3e) and HDL-cholesterol (Fig. 3f) fractions and found that the *Atp10A*$^{-/-}$ mice trend toward having more lipids in these fractions compared to controls, although this did not reach statistical significance. Together, these results show that *Atp10A* deficiency causes female-specific dyslipidemia and changes to lipoprotein metabolism after HFD feeding.

Atp10A deficiency in females causes substantial changes to the plasma lipidome and visceral fat transcriptome after HFD feeding

To get a broader view of the dyslipidemia in the plasma of female *Atp10A*$^{-/-}$ mice, we performed mass spectrometry-based untargeted lipidomics on plasma from female *Atp10A*$^{-/-}$ and *Atp10A*$^{+/+}$ littermates after 12 weeks on HFD after a 5 h fast. We found that *Atp10A* deficiency resulted in statistically significant changes to the abundance of a large number of plasma lipid species; 591 in total, with 324 of these observed from positive ion mode and 267 from negative ion mode lipidomics (Fig. 4a, Study ID ST002696, http://dx.doi.org/https://doi.org/10.21228/M83H7N). To highlight how *Atp10A* deficiency altered specific classes of lipid species, we plotted the log2(Fold Change) of lipid species that were significantly changed and calculated the % of the lipid species in each group that had a positive fold change (increase in abundance, green values) versus a negative fold change (decrease in abundance, blue values) (Fig. 4b). Interestingly, we saw modest increases in the abundance of ATP10A's lipid substrates, PC and hexosylceramides (this includes GlcCer and galactosylceramide (GalCer)). Surprisingly, we observed that plasma eicosanoid, bile acid and fatty acid (FA) conjugate species were dramatically depleted in *Atp10A*$^{-/-}$ mice compared to *Atp10A*$^{+/+}$ littermates.

We further probed the influence of *Atp10A* on metabolism by performing RNAseq on visceral fat (Fig. 4c, NCBI GenBank accession numbers: SRR24233646, SRR24233645). We found that 166 genes were differentially expressed in *Atp10A*$^{-/-}$ compared to *Atp10A*$^{+/+}$ mice, where 29 were downregulated and 137 were upregulated. Some notable differences were substantial increases in expression of *Lipf* and *Pla2g5,* encoding a TG lipase and a secreted phospholipase A_2, respectively, in *Atp10A*$^{-/-}$ mice (Fig. 4c, Supplemental Table 2). Additionally, the orphan G protein-coupled receptor, GPR50, was upregulated 571-fold. This gene has been linked to circulating TG and HDL levels in humans[32], energy metabolism in mice[33], and the attenuation of inflammation and insulin signaling in 3T3-L1 adipocytes[34].

Taken together, these results indicate that ATP10A has a substantial role in lipid metabolism in female mice fed a HFD. The potential mechanistic links between the lipid transport activity of ATP10A and whole-body lipid metabolism are shown in Fig. 4d. Briefly, by translocating PC and GlcCer from the outer leaflet to the inner leaflet of the plasma membrane, ATP10A provides substrates to intracellular lipid metabolism enzymes for production of bioactive lipid signaling molecules while decreasing the availability of PC and GlcCer to molecules in circulation (i.e. lipoproteins, lipases) (Fig. 4d). Thus, this lipid transport could affect levels of PC, GlcCer, and downstream metabolites in the intracellular space and in circulation (Fig. 4b) as well as change the expression levels of lipid handling enzymes (Fig. 4c).

Atp10A deficiency in females results in changes to liver lipid metabolism after HFD feeding

To further probe the impact of *Atp10A* deficiency on lipid metabolism, we measured levels of various lipid species in the liver. We found that female *Atp10A*$^{-/-}$ mice have less liver FFA (Fig. 5a), but no significant differences in the levels of total cholesterol, cholesterol esters (CE), unesterified cholesterol, TG, phospholipids (PL), or ceramides compared to *Atp10A*$^{+/+}$ littermates (Supplemental Fig. 5a–f). Additionally, we measured several different FFA, TG, PL, CE, and ceramide species in the liver, differing in carbon chain lengths and saturation levels (Supplemental Fig. 6). We found that WT mice had higher levels of FFA 16:0 and 18:1w9 compared to KO mice (Supplemental Fig. 6a), while KO mice exhibited elevated levels of CE 18:1w9 compared to WT mice (Supplemental Fig. 6d). Female *Atp10A*$^{-/-}$ mice also exhibit a significant increase in the abundance of monounsaturated vs. saturated species of several TG and PL species (Fig. 5b) and one CE species (Fig. 5c) with carbon chain lengths of 16 and/or 18. Although the total amounts of cholesterol and TG in the liver were not different based on genotype, Oil Red O stained lipid droplets (LD) from the *Atp10A*$^{-/-}$ mice were larger on average compared to *Atp10A*$^{+/+}$ mice (Fig. 5d-f). Therefore, *Atp10A* deficiency results in changes to the amount and saturation state of several lipid species in the liver.

Atp10A deficiency results in changes to liver metabolic signaling

Next, we evaluated potential hepatic mechanisms responsible for the metabolic phenotypes observed in the HFD fed female mice by examining key regulators of energy and lipid metabolism in the liver (Fig. 6f). Diacylglycerol acyltransferases (DGATs) catalyze the final step in TG synthesis (Fig. 6f) and we found that DGAT2

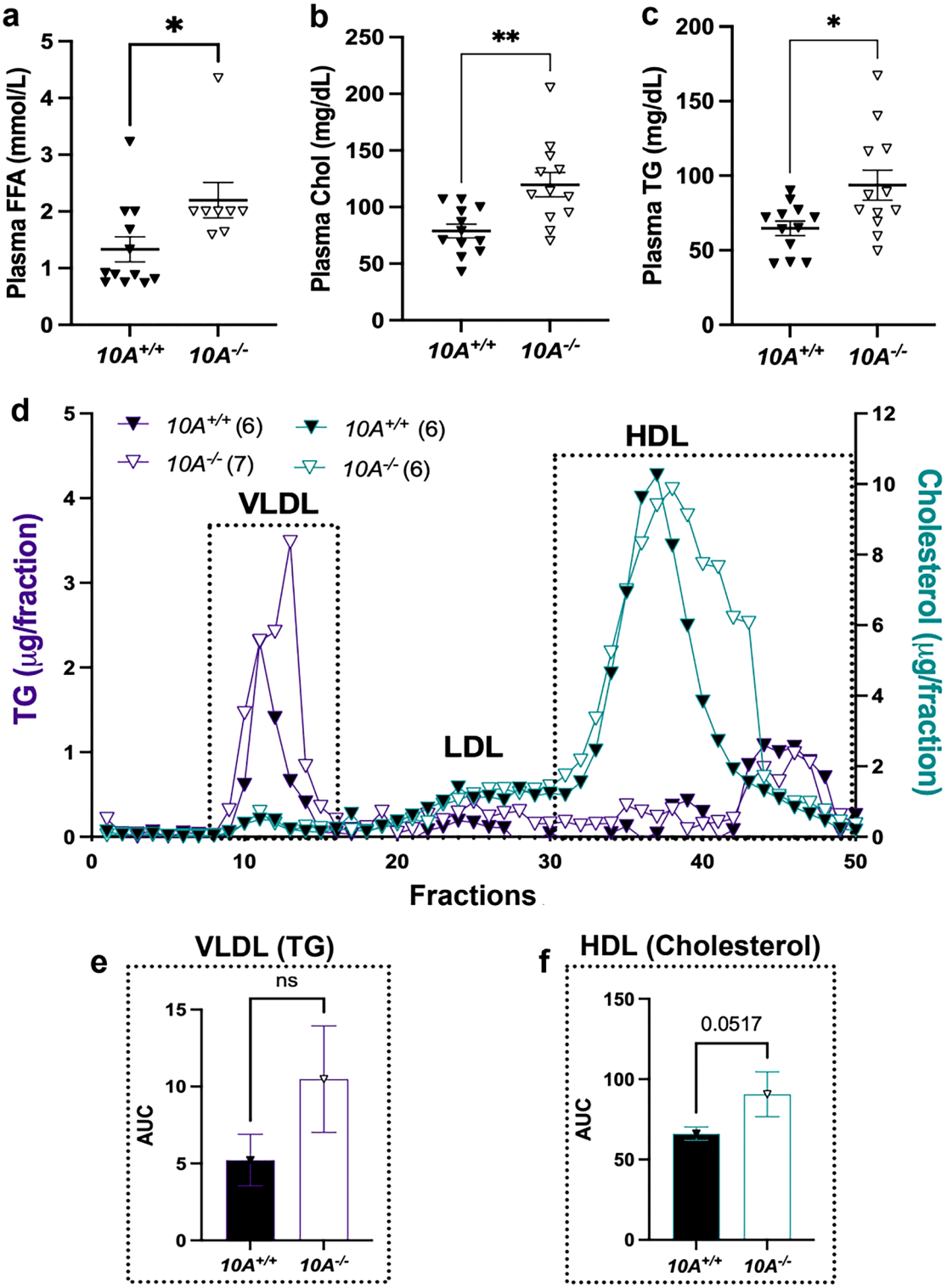

Figure 3. *Atp10A* deletion causes diet-induced dyslipidemia in female mice after 12 weeks of HFD. (**a**–**c**) Free fatty acids (FFA), cholesterol (chol), and triglycerides (TG) were measured in plasma from females after a 5 h fast or after a 5 h fast followed by an OGTT (a, $10A^{+/+}$ n = 12, $10A^{-/-}$ n = 9,*$P = 0.0320$; b, $10A^{+/+}$ n = 12, $10A^{-/-}$ n = 9, **$P = 0.0030$; c, $10A^{+/+}$ n = 12, $10A^{-/-}$ n = 9, *$P = 0.0165$.) (**d**–**f**) Lipoproteins in pooled plasma from females, collected after a 5 h fast or 5 h fast and OGTT, were separated via FPLC. (**e**) Plasma TG (purple) and (**f**) cholesterol (blue) content were measured from the separated lipoproteins. AUC of (**e**) TG fractions 10–18 of VLDL and (**f**) cholesterol fractions 30–50 of HDL (**TG:**$10A^{+/+}$ n = 6, $10A^{-/-}$ n = 7, **Chol:**$10A^{+/+}$ n = 6, $10A^{-/-}$ n = 6). *P* value by unpaired t-test.

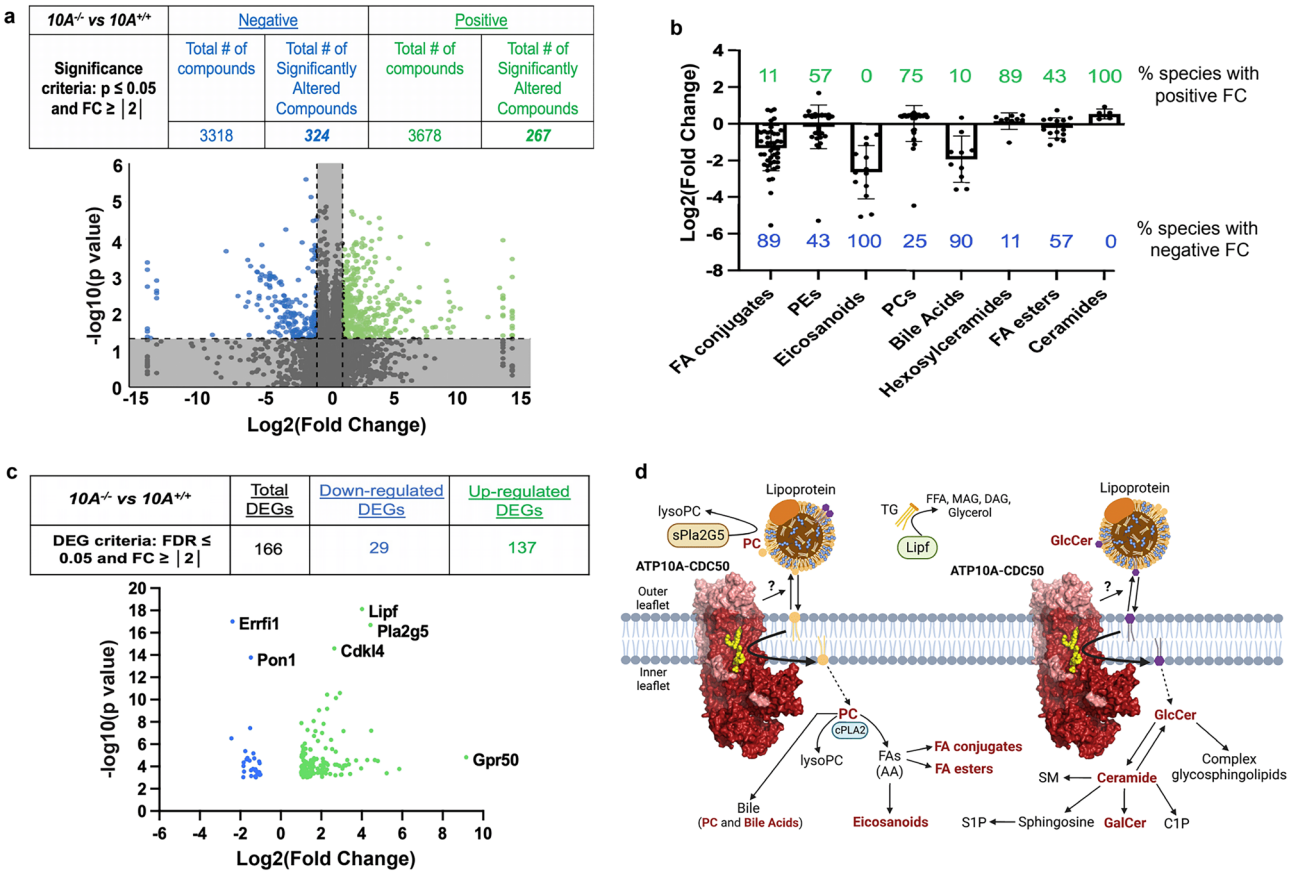

Figure 4. *Atp10A* deletion leads to substantial perturbations in the plasma lipidome and visceral fat transcriptome in female mice on a HFD. (**a**) Lipid metabolites from fasting plasma were measured by HPLC-IM-MS/MS and the data was processed via Progenesis QI. The table indicates the number of total and significantly changed lipid metabolites (compounds) observed from each ionization mode (Negative and Positive); the volcano plot illustrates the fold changes (FC) of compounds between $10A^{-/-}$ vs. $10A^{+/+}$ mice, the grey shading indicates changes that did not meet the significance criteria. P-values by ANOVA. ($10A^{+/+}$ n = 8 , $10A^{-/-}$ n = 8 , see Supplemental Table 3 for complete information about sample size) (**b**) The log2(FoldChange) of lipid metabolites compared between $10A^{-/-}$ vs. $10A^{+/+}$ mice are grouped by indicated categories (green and blue indicate the % of lipid species with positive and negative fold change, respectively, between $10A^{-/-}$ vs. $10A^{+/+}$ mice; P values ≤ 0.1 by ANOVA). (**c**) Sequencing of visceral fat mRNA was performed using the Illumina NovaSeq 6000. The table provides the criteria used to calculate the number of differentially expressed genes (DEGs) and how many DEGs were measured; the volcano plot illustrates the DEGs ($10A^{+/+}$ n = 3,$10A^{-/-}$ n = 3). (**d**) Schematic illustrating the metabolic pathways linking ATP10A substrates to observed changes in the plasma lipidome and visceral fat transcriptome. Lipid metabolites with significant changes due to 10A deletion from panel b are in bold red, the hexosylceramide category includes both GalCer and GlcCer. The protein products from two mRNA transcripts that were significantly upregulated in the visceral fat from $10A^{-/-}$ mice (panel c), Pla2G5 and Lipf, are highlighted to show their role in lipid metabolism. Schematic created using Biorender.com. See Supplemental Table 2 for RNASeq KEGG pathway analysis. PC = phosphatidylcholine, AA = arachidonic acid, TG = triglyceride, FA = fatty acids, FFA = free fatty acids, DAG = diacylglycerol, MAG = monoacylglycerol, SM = sphingomyelin, S1P = sphingosine 1-phosphate, C1P = ceramide 1-phosphate, GalCer = galactosylceramide, GlcCer = glucosylceramide.

was significantly elevated in liver from HFD-fed *Atp10A*$^{-/-}$ females (Fig. 6a,b). These results indicate that the lower liver FFA and larger lipid droplets in the hepatocytes might be due to the higher activity of DGAT2 in *Atp10A*$^{-/-}$ mice. AMP kinase (AMPK) is a central regulator of energy metabolism that inhibits acetyl-CoA carboxylase (ACC) activity by phosphorylating it at S79 (Fig. 6f). Western blot analysis showed that the phosphorylation of AMPK α at T172 and AMPK-dependent inhibitory phosphorylation of ACC at S79 were significantly increased in *Atp10A*$^{-/-}$ females (Fig. 6a,c), which may further contribute to the decreased liver FFA in *Atp10A*$^{-/-}$ mice. Of note, insulin signaling including the activating phosphorylation of the insulin receptor β subunit (IRβ) at Y1146, insulin receptor substrate-1 (IRS-1) at S612, and Akt at S473/T308 were decreased in *Atp10A*$^{-/-}$ mice even though glucose tolerance was not significantly changed (Figs. 6d,e and 2b). Consistent with the changes in insulin signaling, the Akt-dependent inhibitory phosphorylation at GSK-3β at S9 was also decreased in *Atp10A*$^{-/-}$ females (Fig. 6d,e). Cytosolic phospholipase 2 (cPLA$_2$) is an enzyme that catalyzes the hydrolysis of phospholipids, such as PC, to LysoPLs and AA, and AA can be oxidized to form eicosanoids[35].

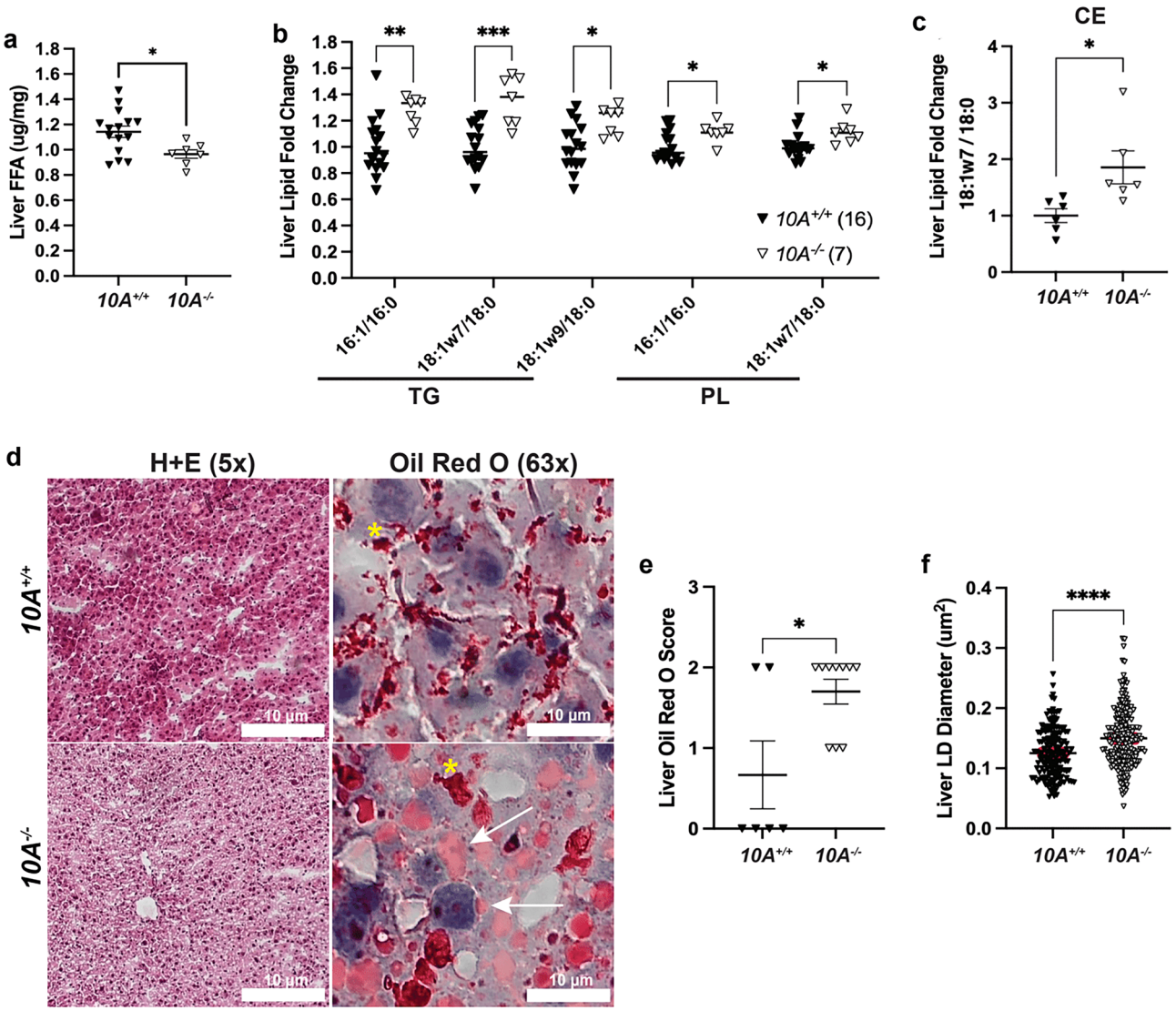

Figure 5. *Atp10A* deletion causes changes to liver lipid metabolism in female mice after 12 weeks of HFD. (**a**) FFAs were measured from flash frozen livers via gas chromatography. Livers were collected after a 5 h fast or after a 5 h fast followed by an OGTT. (FFA: $10A^{+/+}$ n = 15,$10A^{-/-}$ n = 7, *P = 0.0201). The saturation of liver (**b**) TG, PL, and (**c**) CE species was determined by gas chromatography. The fold change of monounsaturated vs saturated TG, PL, CE is shown, **TG**: **P = 0.0025, ***P = 0.0001, *P = 0.0443, **PL**: *P = 0.0297, *P = 0.0281 ($10A^{+/+}$ n = 16, $10A^{-/-}$ n = 7). **CE:** *P = 0.0223 ($10A^{+/+}$ n = 6, $10A^{-/-}$ n = 6). (**d**) Representative images of livers stained with H + E (5x) or Oil Red O (63x). The coalescence of the Oil Red O stain is indicated by yellow asterisks (artifact) and the arrows point to neutral lipids stained by Oil Red O. Scale bars = 10 µM. (**e**) Liver sections were scored using the Oil Red O Score described in the Materials and Methods, *P = 0.0327 ($10A^{+/+}$ n = 6, $10A^{-/-}$ n = 10). (**f**) The diameters of Oil Red O positive lipid droplets (LD) in the liver sections with a score of 2 were measured using ImageJ. The red line in the graph represents the SEM, ****P = < 0.0001 ($10A^{+/+}$,120 LDs measured, n = 2, $10A^{-/-}$, 203 LDs measured, n = 3). P value by (**a**–**c**, **f**) unpaired t-test or (**e**) Mann–Whitney U test.

Interestingly, the activating phosphorylation of $cPLA_2$ at S505 was decreased in the $Atp10A^{-/-}$ mice (Fig. 6d,e), which might contribute to the decreases in eicosanoids in plasma from $Atp10A^{-/-}$ mice (Fig. 4b). Altogether, these studies reveal that *Atp10A* deficiency in females fed a HFD results in several alterations to metabolic signaling in the liver, including depression of the insulin signaling pathway.

Discussion

This study reveals a requirement for ATP10A in protecting female mice from dyslipidemia after HFD feeding. Despite the normal weight gain and body composition (Fig. 1), female $Atp10A^{-/-}$ mice display elevated plasma levels of FFA, cholesterol, and TGs, and these parameters are unchanged in male $Atp10A^{-/-}$ mice relative to WT controls (Fig. 3, Supplemental Fig. 4). The plasma lipidome, visceral fat transcriptome, as well as hepatic lipid metabolism are also substantially perturbed in the knockout female mice (Figs. 4,5). Additionally, basal insulin

signaling in the liver is depressed (Fig. 6) although the plasma insulin levels are comparable to wild-type littermates (Fig. 2d).

Atp10A deficient female mice exhibit dyslipidemia characterized by elevated plasma FFA, cholesterol, TG, and alterations in the size and lipid content of both VLDL and HDL (Fig. 3a–f). A potential source of hyperlipidemia is de novo lipogenesis in the liver; however, *Atp10A* deficient mice exhibit decreased total liver FFAs (Fig. 5a) and an increase in activating phosphorylation of hepatic AMPK α (Fig. 6a,c), a master regulator of lipid metabolism, that increases FA oxidation and decreases de novo lipogenesis through inhibition of ACC[36]. Consistently, we also observed elevated inhibitory AMPKα-dependent phosphorylation of ACC (Fig. 6a,c). Thus, it is unlikely that de novo FA production in the liver is driving the excess plasma TG and FFAs. It is possible that an increased release of FFA from dietary lipids or adipose tissue drives an increase in TG synthesis in the liver and its secretion in VLDL (Fig. 3g)[37–39]. Indeed, we observed an increase in DGAT2 expression in the liver, which could account for the elevated TG. In addition, *Lipf* mRNA transcripts were elevated in visceral fat from *Atp10A* deficient mice (Fig. 4c, Supplemental Table 2). *Lipf* codes for a gastric lipase that breaks down TG into glycerol and FFAs and has been shown to be highly expressed in adipose tissue in a mouse model of diet-induced obesity[40]. It is possible that *Atp10A* deficiency exacerbates this phenomenon, even though the WT and mutant mice exhibit no difference in weight gain or adiposity during high fat diet feeding, via an unknown mechanism.

Loss of ATP10A also disrupts cholesterol metabolism in the female mice. Plasma cholesterol is elevated and the HDL particles carrying the cholesterol are skewed towards smaller sizes. Additionally, *Atp10A* deficient mice show reduced circulating levels of bile acids (Fig. 4a,b), which are important signaling lipids with implications in cholesterol metabolism and cardiovascular health[41]. Further research is needed to understand the mechanisms underlying the perturbations to cholesterol metabolism observed in *Atp10A* deficient mice.

The molecular basis for the female-specific dyslipidemia in *Atp10A*$^{-/-}$ mice is unclear. There are established differences in disease severity and prevalence between men and women[42]. Premenopausal women tend to have lower cardiovascular risks compared to men and there are both hormonal and genetic contributions to sexual dimorphisms in lipid metabolism[43,44]. The *Atp10A* promoter is predicted to have a transcription factor binding site for estrogen receptor alpha (Genecards.org, QIAGEN), so it is possible that differences in expression due to sex contribute to the consequences of *Atp10A* deletion. It is also possible that sex hormones either suppress the effect of *Atp10A*$^{-/-}$ on lipid metabolism in males or promotes these phenotypes in females. We did not measure the lipoprotein profiles, perform plasma lipidomics, examine the composition of plasma or liver lipids, or measure metabolic liver signaling pathways in male mice because they did not exhibit diet-induced dyslipidemia (Supplemental Fig. 4a–c). Interestingly, we found that WT male mice exhibited higher levels of fasting FFA and cholesterol than WT females, suggesting a sex-based difference in the kinetics of lipid clearance during the postprandial response (Fig. 3a–c, Supplemental Fig. 4a–c). There is a need for a comprehensive investigation comparing fasting levels of lipids as well as the composition of the lipids between male and female mice after HFD feeding to uncover potential sexual dimorphisms and elucidate the underlying mechanisms driving such differences.

Interestingly, there is sexual dimorphism in a PC synthesis pathway that exclusively occurs in the liver. In most cells, PC is produced through the CDP-choline pathway (also called the Kennedy pathway) or acylation of LysoPC. However, the liver employs an additional pathway catalyzed by phosphatidylethanolamine N-methyltransferase (PEMT), which converts PE to PC using three methyl groups from S-adenosylmethionine[45]. Interestingly, PEMT activity exhibits sexual dimorphism[46] and the *Pemt* gene is regulated by estrogen[47,48]. Furthermore, *Pemt*$^{-/-}$ mice on a high-fat diet display sex-specific differences in their plasma lipoprotein profiles[49]. Given the role of ATP10A in transporting PC into cells, it is possible that liver PC biosynthetic pathways are overly reliant on the PEMT pathway in *Atp10A* KO mice. It will be interesting to determine if the sexually dimorphic dyslipidemia in the *Atp10A* KO mice is linked to dysregulation of PEMT or to choline deficiency.

Atp10A deficient female mice display elevated levels of monounsaturated versus saturated TG, PL, and cholesterol ester (CE) species in their livers (Fig. 5b,c). This could be due to an increase in activity of stearoyl-CoA desaturase–1 (SCD1), an enzyme that catalyzes the synthesis of monounsaturated FAs from saturated FAs (Fig. 6f). Interestingly, Scd1 activity has been suggested to be required for the onset of diet-induced hepatic insulin resistance[50]. Liver sections from *Atp10A* deficient mice exhibit increased Oil Red O staining, a stain that binds neutral lipids, as well as larger lipid drops compared to control mice (Fig. 5d–f). We observed an increase in the expression of DGAT2 (Fig. 6b) in the liver of *Atp10A* deficient mice, but no significant increase in liver TG (Supplemental Fig. 5d) or cholesterol levels (Supplemental Fig. 5a–c), therefore the increase in Oil Red O staining could be due to staining of another neutral lipid and this needs to be further explored. Furthermore, female *Atp10A* deficient mice display impaired insulin signaling in the liver (Fig. 6) without changes to circulating insulin levels (Fig. 2d), highlighting the need for further exploration to elucidate the relationship between dyslipidemia, liver lipid metabolism, and altered insulin signaling observed in these mice.

Our studies suggest that *Atp10A* deficiency disrupts the regulation of $cPLA_2$ activity and the production of eicosanoids. We found a reduction of activating phosphorylation of $cPLA_2$ in the liver (Fig. 6d,e) as well as a depletion of circulating levels of eicosanoids (Fig. 4a,b) due to ATP10A deficiency. $cPLA_2$ hydrolyzes PC to release AA which can be oxidized to form eicosanoids, bioactive lipids with roles in inflammation and vasculature maintenance[18,51]. $cPLA_2$ can only act on lipids in the cytosolic leaflet and ATP10A could potentially provide additional PC substrate to this enzyme, derived from the extracellular leaflet or an external source, such as lipoproteins. Interestingly, ATP10A can also translocate GlcCer to potentially promote synthesis of ceramide 1-phosphate (C1P) (Fig. 4d), another activator of $cPLA_2$[52]. $cPLA_2$ hydrolysis of PC also produces LysoPC, a bioactive lipid that may link saturated FAs to insulin resistance[53]. Despite the reduction of eicosanoids in the plasma, there was no substantial difference in the levels of circulating LysoPC based on genotype. It is possible that the increased expression of *Pla2g5* (Fig. 4c, Supplemental Table 2), a secreted phospholipase, may have compensated

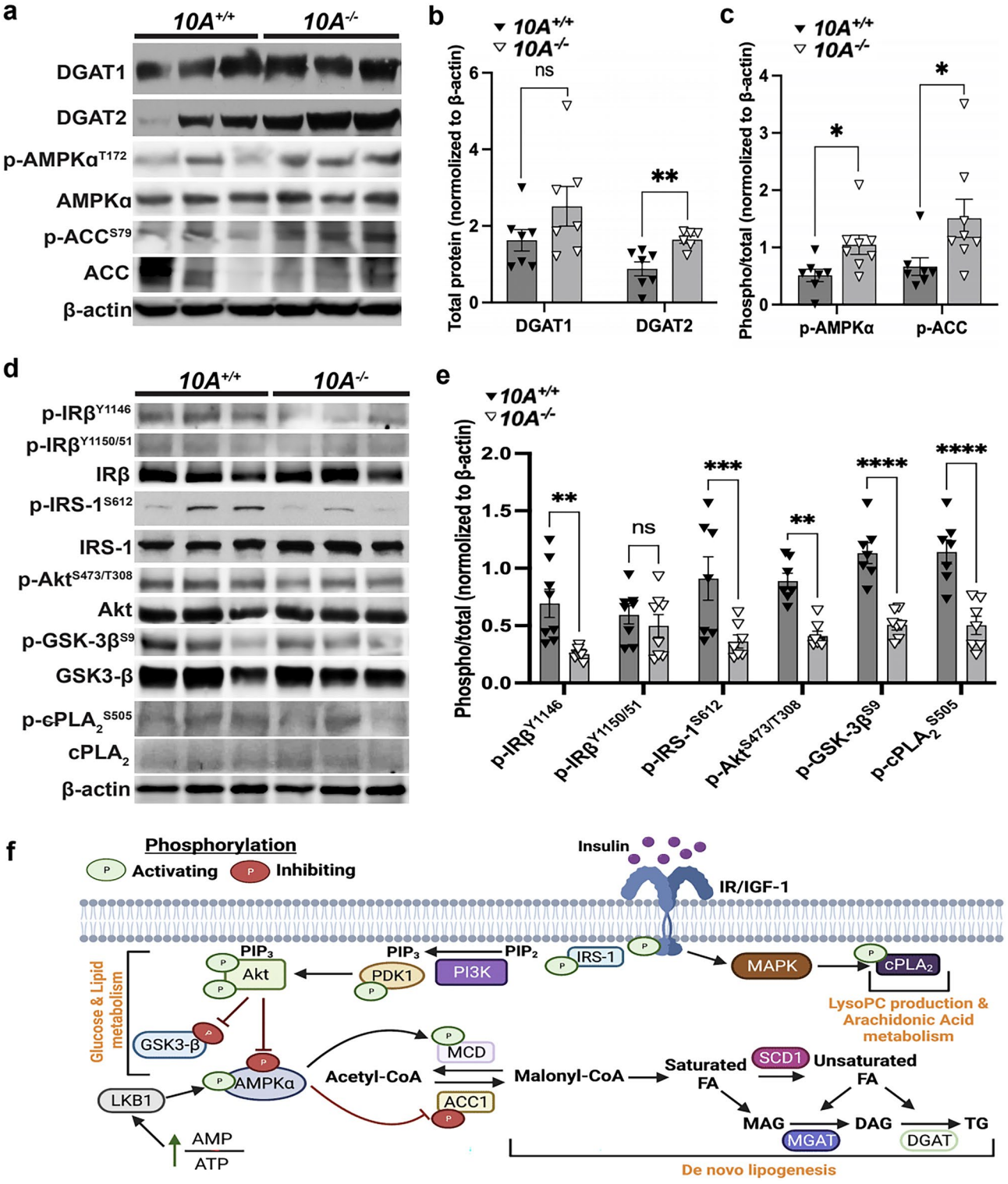

for the perturbations in $cPLA_2$ signaling and normalized LysoPC levels in the plasma. Further work is needed to better define the specific influence of ATP10A on $cPLA_2$ signaling and eicosanoid production in the liver.

Prior studies analyzing mice with an overlapping series of radiation-induced deletions encompassing the *p* locus on chromosome 7 implicated *Atp10A* deficiency in diet-induced obesity, insulin resistance indicated by reduced efficacy of insulin in mediating glucose disposal, and hyperlipidemia, and reported that these phenotypes were more severe in females compared to males[26,27]. Additionally, the phenotypes were observed in heterozygous mice that inherited the chromosomal deletion maternally, suggesting that the paternal *Atp10A* allele was silenced. In support of this possibility, we found that heterozygous male mice inheriting the *Atp10A* exon 2 deletion maternally displayed a trend toward increased weight gain over the course of the HFD and had significantly shorter bodies and elevated fasting blood glucose compared to mice that inherited the deletion

◂**Figure 6.** *Atp10A* deletion perturbs liver insulin signaling in female mice fed a HFD. (**a**, **d**) Representative blots for total and/or phosphorylated (**a**) DGAT1, DGAT2, AMPKα, ACC, and (**d**) IRβ, IRS-1, Akt, GSK-3β, and $cPLA_2$. (**b**) For DGAT1 and DGAT2 quantitation, total protein was normalized to β-actin levels. (**c**, **e**) The phosphoproteins were normalized to their respective total protein and β-actin levels. Mean measurements of 4–6 independent experiments are shown. *P* value by (**b**, **c**) unpaired t-test or (**e**) 2-way ANOVA with Sidak's multiple comparison test. (**a**–**c**, $10A^{+/+}$ n = 7, $10A^{-/-}$ n = 7, **b**: $^{**}P = 0.0050$; **c**: $^{*}P = 0.0229$, $^{*}P = 0.0481$; **d**, **e**, $10A^{+/+}$ n = 8, $10A^{-/-}$ n = 8, $^{**}P = 0.0044$, $^{***}P = 0.0007$, $^{**}P = 0.0038$, $^{****}P =< 0.0001$,). (a) Original blots are shown in Supplemental Fig. 7B (DGAT 1 and DGAT 2) and Supplemental Fig. 7C (ACC, p-AMPKα^{T172}, p-ACC^{S79}, AMPKα, β-actin. (**b**) Original blots are shown in Supplemental Fig. 7D (p-IRβ^{1146}, p-IRβ$^{1150/51}$), Supplemental Fig. 7E (p-GSK-3β^{S9}, p-$cPLA_2$^{S505}, $cPLA_2$, IRβ), Supplemental Fig. 7F (p-IRS-1^{S612}, IRS-1), Supplemental Fig. 7G (p-Akt$^{S473/T308}$, Akt, GSK-3β), Supplemental Fig. 7H (β-actin). (**f**) Schematic adapted from[65] and created using Biorender.com. The illustration shows insulin binding to the insulin receptor and the resulting downstream signaling events that stimulate LysoPC production, AA metabolism, changes to glucose and lipid metabolism; including the promotion of lipogenesis. MAPK = mitogen-activated protein kinase, $cPLA_2$ = cytosolic phospholipase 2, IRS-1 = insulin receptor substrate 1, PI3K = phosphoinositide 3-kinase, PIP2 = phosphatidylinositol 4,5-bisphosphate, PIP3 = phosphatidylinositol 3,4,5-triphosphate, PDK1 = pyruvate dehydrogenase kinase 1, GSK-3β = glycogen synthase kinase-3 beta, LKB1 = liver kinase B1, AMPKα = AMP-activated protein kinase alpha, MCD = malonyl-CoA decarboxylase, ACC1 = acetyl-CoA carboxylase, SCD1 = stearoyl-CoA desaturase 1, MGAT = monoglycerol acyltransferase, DGAT = diglyceride acyltransferase.

paternally (Supplemental Fig. 3a,d,e). However, we found no evidence for increased obesity or metabolic defects in female $Atp10A^{+/-}$ heterozygous mice inheriting the KO allele paternally or maternally (Supplemental Fig. 3), nor did the $Atp10A^{-/-}$ homozygous mice display alterations to the development of diet-induced obesity or defects in glucose metabolism (Figs. 1, 2). This difference is most likely because the mice used in previous studies had a large chromosomal deletion that, in addition to *Atp10A*, removed several other genes, some of which are known to be imprinted[54]. It is also possible that differences in the strain background or rearing environment alter the susceptibility of *Atp10A* deficient mice to weight gain on a HFD and glucose metabolism perturbations. However, our results are consistent with previous reports in that ATP10A has a stronger influence on lipid metabolism in female mice relative to males[26]. We have shown that ATP10A is required to maintain lipid homeostasis and liver insulin sensitivity with HFD feeding, therefore, a therapeutic that acts as an ATP10A agonist could help treat diseases that cause dyslipidemia and hepatic insulin resistance.

Methods

Animals

All mouse experiments were approved under the Vanderbilt University Institutional Animal Care and Use Committee. Mice were housed in 12 h light/dark cycles in temperature and humidity-controlled facilities with ad-libitum access to diet and water. Mice in this study were sacrificed via CO_2 euthanasia systems, operating at the recommended flow rates, followed by cervical dislocation; this method is an acceptable euthanasia method according to the American Veterinary Medical Association (AVMA) guidelines. The mouse studies described in this manuscript are reported in accordance with the ARRIVE guidelines (https://arriveguidelines.org/).

Randomization

Experimental mice were generated using het x het breeding schemes (or het x WT schemes for the inheritance studies). WT and KO (or paternal inheritance and maternal inheritance) mice were assigned to studies as they became available from the breeding process. In order to allocate mice for in vivo experiments conducted over multiple days, an online list randomizer (https://www.random.org/) was employed. This tool was used to randomize lists of mouse IDs, and the allocation of mice to specific experiment days was based on the outcomes of these randomized lists.

Creating the mouse model

The *Atp10A* mouse model (knockout allele name: *Atp10Aem1(Vtrg)*) was created via CRISPR-Cas9 in collaboration with the Vanderbilt Genome Editing Resource. Guide RNAs (crRNA) were created to target *Atp10A* on chromosome 7: Target Intron 1–2: TGACTGCTTAATGATTCGAGG, GAGTGACTGCTAATGATCG, Target Intron 2–3: GGAAAAAGCCCAATTCCACAC, AGCCCAATCCACACAGGAAC. CRISPR editing reagents were delivered into the pronuclei of one-cell fertilized mouse zygotes (C57BL/6J). Approximately 608 bp were deleted using this method: nucleotides 58,389,679–58,390,287 (NCBI reference sequence: NC_000073). The resulting pups were biopsied and screened by PCR and Sanger sequencing. The predicted founders were bred to WT C57BL/6J animals and the offspring were genotyped (N1 generation). The offspring with the appropriate genotype were then backcrossed two more times.

Genotyping

Mice were genotyped using tail DNA. *Atp10A* DNA products were detected via PCR (Q5 DNA Polymerase, NEB) followed by gel electrophoresis; *Atp10A-F* (GTGCACTGTATTTGTCTGCCTGTTCC), *Atp10A-R* (GGTCCT TTGAAGAGATAATGTTCCCAAC). PCR samples were purified (QIAquick spin column (lot No. 166028242)) and sent to Genewiz (https://www.genewiz.com/) for sequencing.

Body composition, body length, and tissue mass

WT and experimental mice were fed standard chow or 60% HFD (D12492, Research Diets) ad libitum, starting at the age of 3–12 weeks old (see Supplemental Table 3). Mice were weighed once per week to measure body weight gain over time. On the 12th week on the HFD, body composition was assessed via NMR (LF50 Body Composition Mice Analyzer, Bruker, stock # E140000501). Mice were sacrificed with CO_2, the body lengths were measured and the mass of the wet tissue was measured using an analytical scale. Tissues were collected and flash frozen when mice were sacrificed.

Blood collection

Blood was taken from tail-veins, retroorbital bleeds, or cardiac punctures (for each method described here, the blood collection method is reported). Mice were awake and being monitored for signs of stress when tail blood was taken. Tail blood was collected using EDTA tubes (Sarstedt, Microvette CB 300 K2E, order # 16.444.100) and spun down at 4 °C at full speed for 2 min. Before retroorbital bleeds were taken, mice were anesthetized for 1 min via inhalation of Isoflurane via the SomnoFlo Low-Flow Electronic Vaporizer (Kent Scientific Corporation) operating at the settings approved by the IACUC protocol and mice were closely monitored during this procedure. For cardiac punctures, mice were first sacrificed using CO_2 euthanasia systems followed by cervical dislocation. Retroorbital blood and cardiac puncture blood were placed into tubes containing 5 uL of 0.5 M EDTA and centrifuged at 4 °C at 2000 rcf for 15 min.

Oral glucose tolerance tests (OGTT) and fasting blood glucose/insulin measurements

Researchers were blind to the genotype of the mice during the OGTT. Mice were fasted for 5 h (7AM–12PM) and then fasting blood was collected via retroorbital bleeds and mice were allowed to wake up and fully recover before the start of the OGTT. The mice were then gavaged with 20% w/v dextrose (final 2 g/kg body weight), and a tail-vein blood glucose was measured via a glucometer (Accu-Chek, Accu-Chek Aviva Plus Meter) at baseline, 15, 30, 45, 60, 90, and 120 min. The area under of the curve for glucose was calculated using GraphPad Prism. Insulin from plasma samples collected from 5 h fasted mice via the retroorbital bleed were measured using the Crystal Chem Ultrasensitive Mouse Insulin ELISA Kit (catalog # 90080).

Plasma lipid and lipoprotein analysis

Plasma was collected, via a retroorbital bleed or cardiac puncture, from 5 h fasted mice and 5 h fasted mice that had undergone an OGTT (see Supplemental Table 3).For males and a portion of the female samples: plasma TG and cholesterol were measured using colorimetric kits (note that the TG measurements include free glycerol) (Inifinity, Thermo Scientific, TG catalog #TR22421, chol catalog #TR13421) and plasma FFAs were measured using Abcam's Free Fatty Acid Assay Kit-Quantification (ab65341). For the rest of the females: plasma samples were measured by the Vanderbilt Hormone Assay and Analytical Services Core, where plasma cholesterol and TG were measured by standard enzymatic assays, and plasma FFAs were analyzed with an enzymatic kit (Fujifilm Healthcare Solutions, catalog #999-34691). Lipoproteins were separated using FPLC on a Superose6 column (GE Healthcare) from 150 µl plasma (single mouse or pooled) and the TG and cholesterol content were measured using colorimetric kits (Inifinity, Thermo Scientific, TG catalog #TR22421, chol catalog #TR13421). AUC was calculated using GraphPad Prism.

Plasma lipidomics

Plasma was collected, via a retroorbital bleed or cardiac puncture, from 5 h fasted mice and some samples are pooled plasma (see Supplemental Table 3). Lipid metabolites were extracted from 100 µL plasma by methyl *tert*-butyl ether.

(MTBE) extraction

The lipid metabolites were then analyzed by HPLC-IM-MS/MS on an Agilent 6560 mass spectrometer using a ZORBAX Extend-C18 RPLC column (Phase A: 0.1% formic acid and 10 mM NH_4CHOO in water, Phase B: 0.1% formic acid and 10 mM NH_4CHOO in 60:36:4 isopropanol:acetonitrile: H_2O)[55]. Data alignment and biostatical analysis was performed using Progenesis QI (Waters). Tentative compound identifications were assigned using accurate mass databases and a previously described ion mobility-based filtering method[56–58].

RNA Sequencing

Visceral fat was collected from mice after CO_2 sacrifice and cervical dislocation and was flash frozen in liquid nitrogen and then kept at − 80 °C until thawed at − 20 °C in RNA*later* (ThermoFisher, catalog # AM7030). The tissue was then homogenized in QIAzol Lysis Reagent (Qiagen, catalog #79306) using a Bullet Blender (Next Advance, BT24M). The RNA layer acquired after the QIAzol Lysis protocol was cleaned up using the RNeasy Lipid Tissue Mini Kit (Qiagen, catalog #NC9036170). Quality control measurements and Next Generation Sequencing (NGS) was performed on 20 uL of RNA (> 10 ng) by Vanderbilt Technologies for Advanced Genomics (VANTAGE); briefly, NEBNext Ultra II Directional RNA kit (Cat no: E7760L) was used and for the sequencing; NovaSeq 6000 and PE150 read lengths were used. Analysis of NGS data was performed by Vanderbilt Technologies for Advanced Genomics Analysis and Research Design (VANGARD). RNA sequencing data was also analyzed using the KEGG Database, developed by Kanehisa Laboratories[59–61].

Immunoblot analysis

Western blots were initially performed and quantified blinded to the genotype. After unblinding, samples were grouped by genotype and re-run for presentation of the data. Liver was collected from mice after CO_2 sacrifice and cervical dislocation and was flash frozen in liquid nitrogen and then kept at − 80 °C until further processing. For lysis of liver tissue samples, T-PER (Pierce, Rockford, IL) with phosphatase and protease inhibitors (Sigma) was used. Protein concentration was quantified using BCA Reagent (Pierce, Rockford, IL). Protein extracts (100 µg) were subjected to Western immunoblot analysis. The following primary antibodies were used for detection of: DGAT1 (sc-32861, Santa Cruz Biotech), DGAT2 (sc-66859, Santa Cruz Biotech), phospho-AMPKα^{T172} (#2535, Cell Signaling), AMPKα (#2532, Cell Signaling), phospho-ACC^{S79} (#3661, Cell Signaling), ACC (#3676, Cell Signaling) , phospho-IGF-IRβ^{Y1131}/IRβ^{Y1146} (#3021, Cell Signaling), phospho-IGF-IRβ$^{Y1135/1136}$/IRβ$^{Y1150/1151}$(#3024, Cell Signaling), IRβ (#3025, Cell Signaling), phospho-IRS-1^{S612} (#3203, Cell Signaling), IRS-1 (#3407, Cell Signaling), phospho-Akt$^{T308/S473}$ (#13038/#4060, Cell Signaling), Akt (#9272, Cell signaling), phospho-GSK-3β^{S9} (#5558, Cell Signaling), GSK-3β (#9315, Cell Signaling), phospho-cPLA$_2$α^{S505}(#53044, Cell Signaling), cPLA$_2$α (#5249, Cell Signaling). Antibody to β-actin (#4970, Cell Signaling) was used to evaluate protein loading in each lane. Immunoblots were developed using the Western Lightning Chemiluminescence Plus detection system (PerkinElmer, Wellesley, MA) according to the manufacturer's protocol. Intensity of the immunoblot bands was measured using AI600 CCD Imager for chemiluminescent assays (Amersham). Densitometry was performed using ImageJ. For quantification, OD of bands for phosphoprotein was normalized to total protein and β-actin; otherwise, OD of bands for total protein was normalized to β-actin.

Promethion system

Indirect calorimetry and additional measures of food intake and physical activity were performed in open-circuit indirect calorimetry cages (Promethion System, Sable Systems International) at Vanderbilt Mouse Metabolic Phenotyping Center (MMPC). One week prior to the experiment start date, mice were singly housed for acclimation. On the day of the experiment start date, mice were weighed and body composition was assessed. The mice were placed in the cages of the Promethion system, one mouse per cage. The cages were housed in a light and temperature-controlled chamber. The light cycle was set on a 12:12 h cycle (6am–6 pm). Mice were left undisturbed for 5 days during which all the measurements were made. The system periodically measured rates of O_2 consumption (VO_2) and CO_2 production (VCO_2) for each cage, as well as food intake and physical activity (infrared beam array). Data were processed in time segments (daily 24 h, and 12 h dark/12 h light), and averages calculated for each as well as for the 24 h period. After 5 days, the mice were removed from the cages, and body composition and weight were measured again. Data was further processed using CalR (www.calrapp.org).

Measuring liver lipids

Liver was collected from mice after CO_2 sacrifice and cervical dislocation and was flash frozen in liquid nitrogen and then kept at − 80 °C until further processing. Liver FFA, total cholesterol, cholesterol ester, unesterified cholesterol, TG, PLs, and ceramides were measured by the Vanderbilt Hormone Assay and Analytical Services Core. Briefly; lipids were extracted using the method of Folch-Lees[62]. The extracts were filtered and lipids recovered in the chloroform phase. Individual lipid classes were separated by thin layer chromatography using Silica Gel 60 A plates developed in petroleum ether, ethyl ether, acetic acid (80:20:1) and visualized by rhodamine 6G. Phospholipids, triglycerides and cholesteryl esters were scraped from the plates and methylated using BF_3 / methanol as described by Morrison and Smith[63]. The methylated fatty acids were extracted and analyzed by gas chromatography. Gas chromatographic analyses were carried out on an Agilent 7890A gas chromatograph equipped with flame ionization detectors and a capillary column (SP2380, 0.25 mm × 30 m, 0.20 µm film, Supelco, Bellefonte, PA). Helium was used as the carrier gas. The oven temperature was programmed from 160 to 230 °C at 4 °C/min. Fatty acid methyl esters are identified by comparing the retention times to those of known standards. Inclusion of lipid standards with odd chain fatty acids permits quantitation of the amount of lipid in the sample. Dipentadecanoyl phosphatidylcholine (C15:0), diheptadecanoin (C17:0), trieicosenoin (C20:1), and cholesteryl eicosenoate (C20:1) were used as standards.

Oil Red O

Liver was collected from mice after CO_2 sacrifice and cervical dislocation and then placed in frozen section medium (Epredia, Neg-50, catalog #22-110-617) and then on dry ice. When the frozen section medium was solidified, the livers were placed at − 20 °C until further processing. Further processing was done by the Vanderbilt Translation Pathology Shared Resource (TPSR): Slides were brought to room temperature and placed in 10% NBF solution for 10 min. The Newcomer Supply Tech Oil Red O, Propylene Glycol staining kit (Newcomer Supply, catalog # 12772B) was used for visualization. Slides were then cover slipped with aqueous mounting medium. In regard to Oil Red O scoring: Dr. Katherine Gibson Corley, a board-certified veterinary pathologist at the Vanderbilt TPSR, created the scoring system used to score the Oil Red O stained liver sections. The scoring system is characterized by: 0 = no Oil Red O staining, 1 = rare and scattered Oil Red O staining, 2 = multi-focal and coalescing Oil Red O staining, 3 = diffuse Oil Red O staining (in whole tissue). To score the slides, the scorer was blinded to the slide IDs and then scored the slides twice, on two separate days. Then the scores from both days were compared and if they did not match, the scorer viewed the slide again and decided on a final score. The diameter of the Oil Red O positive lipid droplets was measured from slides with a score of 2, using ImageJ. Images of tissues were acquired using light microscopy (Zeiss AxioPlan, Upright Fluorescence Microscope, Germany) with a × 5/1.0 or × 63/1.0 Oil using the Zeiss Axio Color Camera (Axiocam 208c) and the ZEN 3.1 software (blue edition). Microscope settings were held constant for all experimental groups.

Statistics

All statistical analysis was done using GraphPad Prism, version 9.5.0 (GraphPad Software). Error bars indicate mean with standard error of the mean (SEM). When more than 2 groups were compared, a 2-way ANOVA was used with Dunnett's correction for multiple comparisons with a control group. Šidák's correction was used for comparison of groups of means. Differences between group mean values were tested using a 2-tailed Student's *t* test or a Mann–Whitney *U* test for nonparametric data. A *P* value of less than 0.05 was considered statistically significant. The number of experimental animals needed was determined from pilot studies and subsequent power calculations (G* power, Heinrich Heine Universitat Dusseldorf); acceptable power was 0.8 or higher.

Ethical approval

The animal protocol was approved by Vanderbilt University Medical Center and IACUC and all methods were performed in accordance with the relevant guidelines and regulations.

Data availability

The untargeted lipidomics data is available at the NIH Common Fund's National Metabolomics Data Repository (NMDR) website, the Metabolomics Workbench[64], where it has been assigned Study ID ST002696. The data can be accessed directly via its Project DOI: https://doi.org/10.21228/M83H7N. The reads from the RNASeq data can be found at NCBI (https://www.ncbi.nlm.nih.gov/genbank/samplerecord/) using these accession numbers: SRR24233646 (*Atp10A* WT reads) and SRR24233645 (*Atp10A* KO reads).

Received: 11 August 2023; Accepted: 19 December 2023
Published online: 03 January 2024

References

1. Aguilar, M., Bhuket, T., Torres, Liu, B. & Wong, R. J. Prevalence of the metabolic syndrome in the United States, 2003–2012. *JAMA* **313**(19), 1973–1974. https://doi.org/10.1001/jama.2015.4260 (2015).
2. O'Neill, S. & O'Driscoll, L. Metabolic syndrome: A closer look at the growing epidemic and its associated pathologies. *Obes. Rev.* **16**(1), 1–12. https://doi.org/10.1111/obr.12229 (2015).
3. Fahed, G. *et al.* Metabolic syndrome: Updates on pathophysiology and management in 2021. *Int. J. Mol. Sci.* **23**, 786. https://doi.org/10.3390/ijms23020786 (2022).
4. Arnett, D. K. Genome-wide detection of allele specific copy number variation associated with insulin resistance in African Americans from the hyperGEN study. *PLoS ONE* https://doi.org/10.1371/journal.pone.0024052 (2011).
5. Kengia, J. T. *et al.* A gene variant in the Atp10d gene associates with atherosclerotic indices in Japanese elderly population. *Atherosclerosis* **231**(1), 158–162. https://doi.org/10.1016/j.atherosclerosis.2013.08.034 (2013).
6. Andersen, J. P. *et al.* P4-ATPases as phospholipid flippases-structure, function, and enigmas. *Front. Physiol.* https://doi.org/10.3389/fphys.2016.00275 (2016).
7. Segawa, K. *et al.* Caspase-mediated cleavage of phospholipid flippase for apoptotic phosphatidylserine exposure. *Science* https://doi.org/10.1126/science.1252809 (2014).
8. Kook, S. *et al.* AP-3-dependent targeting of flippase ATP8A1 to lamellar bodies suppresses activation of YAP in alveolar epithelial type 2 cells. *Proc. Natl. Acad. Sci. U. S. A.* **118**(20), e2025208118. https://doi.org/10.1073/pnas.2025208118 (2021).
9. Ristovski, M., Farhat, D., Bancud, S. E. M. & Lee, J. Y. Lipid transporters beam signals from cell membranes. *Membranes* **11**, 562. https://doi.org/10.3390/membranes11080562 (2021).
10. van der Mark, V. A., Oude Elferink, R. P. J. & Paulusma, C. C. P4 ATPases: Flippases in health and disease. *Int. J. Mol. Sci.* https://doi.org/10.3390/ijms14047897 (2013).
11. Naito, T. *et al.* Phospholipid flippase ATP10A translocates phosphatidylcholine and is involved in plasma membrane dynamics. *J. Biol. Chem.* **290**(24), 15004–15017. https://doi.org/10.1074/jbc.M115.655191 (2015).
12. Roland, B. P. *et al.* Yeast and human P4-ATPases transport glycosphingolipids using conserved structural motifs. *J. Biol. Chem.* https://doi.org/10.1074/jbc.RA118.005876 (2019).
13. Ramos-Martín, F. & D'Amelio, N. Biomembrane lipids: When physics and chemistry join to shape biological activity. *Biochimie* **203**, 118–138. https://doi.org/10.1016/j.biochi.2022.07.011 (2022).
14. Law, S. H. *et al.* An updated review of lysophosphatidylcholine metabolism in human diseases. *Int. J. Mol. Sci.* **20**, 1149. https://doi.org/10.3390/ijms20051149 (2019).
15. Knuplez, E. & Marsche, G. An updated review of pro-and anti-inflammatory properties of plasma lysophosphatidylcholines in the vascular system. *Int. J. Mol. Sci.* **21**, 4501. https://doi.org/10.3390/ijms21124501 (2020).
16. Liu, P. *et al.* The mechanisms of lysophosphatidylcholine in the development of diseases. *Life Sci.* **247**, 117443. https://doi.org/10.1016/j.lfs.2020.117443 (2020).
17. Yamaguchi, A., Botta, E. & Holinstat, M. Eicosanoids in inflammation in the blood and the vessel. *Front. Pharmacol.* **13**, 997403. https://doi.org/10.3389/fphar.2022.997403 (2022).
18. Mitchell, J. A. & Kirkby, N. S. Eicosanoids, prostacyclin and cyclooxygenase in the cardiovascular system. *Br. J. Pharmacol.* **176**, 1038–1050. https://doi.org/10.1111/bph.14167 (2019).
19. Ishibashi, Y., Kohyama-Koganeya, A. & Hirabayashi, Y. New insights on glucosylated lipids: Metabolism and functions. *Biochim. Biophys. Acta-Mol. Cell Biol. Lipids* **1831**, 1475–1485. https://doi.org/10.1016/j.bbalip.2013.06.001 (2013).
20. Mobarak, E. *et al.* Glucosylceramide modifies the LPS-induced inflammatory response in macrophages and the orientation of the LPS/TLR4 complex in silico. *Sci. Rep.* **8**(1), 13600. https://doi.org/10.1038/s41598-018-31926-0 (2018).
21. Aerts, J. M. *et al.* Pharmacological inhibition of glucosylceramide synthase enhances insulin sensitivity. *Diabetes* **56**(5), 1341–1349. https://doi.org/10.2337/db06-1619 (2007).
22. Baccam, G. C. *et al.* Glucosylceramide synthase inhibition protects against cardiac hypertrophy in chronic kidney disease. *Sci. Rep.* **12**, 9340. https://doi.org/10.1038/s41598-022-13390-z (2022).
23. Bikman, B. T. & Summers, S. A. Ceramides as modulators of cellular and whole-body metabolism. *J. Clin. Investig.* **121**, 4222–4230. https://doi.org/10.1172/JCI57144 (2011).
24. Turpin-Nolan, S. M. & Brüning, J. C. The role of ceramides in metabolic disorders: When size and localization matters. *Nat. Rev. Endocrinol.* **16**, 224–233. https://doi.org/10.1038/s41574-020-0320-5 (2020).
25. Sandhoff, R., Schulze, H. & Sandhoff, K. Chapter one—Ganglioside metabolism in health and disease. In *Progress in Molecular Biology and Translational Science* Vol. 156 (eds Schnaar, R. L. & Lopez, P. H. H.) 1–62 (Academic Press, 2018).
26. Dhar, M. S. *et al.* Mice heterozygous for Atp10c, a putative amphipath, represent a novel model of obesity and type 2 diabetes. *J. Nutr.* **134**(4), 799–805. https://doi.org/10.1093/jn/134.4.799 (2004).

27. Dhar, M. S., Yuan, J. S., Elliott, S. B. & Sommardahl, C. A type IV P-type ATPase affects insulin-mediated glucose uptake in adipose tissue and skeletal muscle in mice. *J. Nutr. Biochem.* https://doi.org/10.1016/j.jnutbio.2006.01.002 (2006).
28. Kayashima, T., Ohta, T., Niikawa, N., Kishino, T. & Oshimura, M. On the conflicting reports of imprinting status of mouse ATP10a in the adult brain: Strain-background-dependent imprinting? (multiple letters). *J. Hum. Genet.* **48**, 492–493. https://doi.org/10.1007/s10038-003-0061-z (2003).
29. Hogart, A., Patzel, K. A. & LaSalle, J. M. Gender influences monoallelic expression of ATP10A in human brain. *Hum. Genet.* **124**(3), 235–242. https://doi.org/10.1007/s00439-008-0546-0 (2008).
30. DuBose, A. J., Johnstone, K. A., Smith, E. Y., Hallett, R. A. E. & Resnick, J. L. Atp10a, a gene adjacent to the PWS/AS gene cluster, is not imprinted in mouse and is insensitive to the PWS-IC. *Neurogenetics* https://doi.org/10.1007/s10048-009-0226-9 (2010).
31. Hurst, S. E., Minkin, S. C., Biggerstaff, J. & Dhar, M. S. Transient silencing of a type IV P-type ATPase, Atp10c, results in decreased glucose uptake in C2C12 myotubes. *J. Nutr. Metab.* https://doi.org/10.1155/2012/152902 (2012).
32. Bhattacharyya, S. *et al.* Sequence variants in the melatonin-related receptor gene (GPR50) associate with circulating triglyceride and HDL levels. *J. Lipid Res.* **47**(4), 761–766. https://doi.org/10.1194/jlr.M500338-JLR200 (2006).
33. Ivanova, E. A. *et al.* Altered metabolism in the melatonin-related receptor (GPR50) knockout mouse. *Am. J. Physiol. Endocrinol. Metab.* **294**(1), E176–E182. https://doi.org/10.1152/ajpendo.00199.2007 (2008).
34. Yao, Z. *et al.* Orphan receptor GPR50 attenuates inflammation and insulin signaling in 3T3-L1 preadipocytes. *FEBS Open Bio* **13**(1), 89–101. https://doi.org/10.1002/2211-5463.13516 (2023).
35. Niknami, M., Patel, M., Witting, P. K. & Dong, Q. Molecules in focus: Cytosolic phospholipase A2-α. *Int. J. Biochem. Cell Biol.* **41**, 994–997. https://doi.org/10.1016/j.biocel.2008.07.017 (2009).
36. Garcia, D. & Shaw, R. J. AMPK: Mechanisms of cellular energy sensing and restoration of metabolic balance. *Mol. Cell* **66**, 789–800. https://doi.org/10.1016/j.molcel.2017.05.032 (2017).
37. Barter, P. J. & Nestel, P. J. Precursors of plasma triglyceride fatty acids in obesity. *Metabolism* **22**(6), 779–785. https://doi.org/10.1016/0026-0495(73)90048-6 (1973).
38. Kissebah, A. H., Alfarsi, S., Adams, P. W. & Wynn, V. Role of insulin resistance in adipose tissue and liver in the pathogenesis of endogenous hypertriglyceridaemia in man. *Diabetologia* **12**(6), 563–571. https://doi.org/10.1007/BF01220632 (1976).
39. Lewis, G. F. Lipid metabolism. *Curr. Opin. Lipidol.* **10**(5), 475–477 (1999).
40. Sato, H. *et al.* The adipocyte-inducible secreted phospholipases PLA2G5 and PLA2G2E play distinct roles in obesity. *Cell Metab.* **20**(1), 119–132. https://doi.org/10.1016/j.cmet.2014.05.002 (2014).
41. Hanafi, N. I., Mohamed, A. S., Kadir, S. H. S. A. & Othman, M. H. D. Overview of bile acids signaling and perspective on the signal of ursodeoxycholic acid, the most hydrophilic bile acid, in the heart. *Biomolecules* **8**, 159. https://doi.org/10.3390/biom8040159 (2018).
42. Crimmins, E. M., Shim, H., Zhang, Y. S. & Kim, J. K. Differences between men and women in mortality and the health dimensions of the morbidity process. *Clin. Chem.* **65**, 135–145. https://doi.org/10.1373/clinchem.2018.288332 (2019).
43. Palmisano, B. T., Zhu, L., Eckel, R. H. & Stafford, J. M. Sex differences in lipid and lipoprotein metabolism. *Mol. Metab.* **15**, 45–55. https://doi.org/10.1016/j.molmet.2018.05.008 (2018).
44. Link, J. C. & Reue, K. Genetic basis for sex differences in obesity and lipid metabolism. *Annu. Rev. Nutr.* **37**, 225–245. https://doi.org/10.1146/annurev-nutr-071816-064827 (2017).
45. Vance, D. E. & Ridgway, N. D. The methylation of phosphatidylethanolamine. *Prog. Lipid Res.* **27**(1), 61–79. https://doi.org/10.1016/0163-7827(88)90005-7 (1988).
46. Johnson, P. I. & Blusztajn, J. K. Sexually dimorphic activation of liver and brain phosphatidylethanolamine N-methyltransferase by dietary choline deficiency. *Neurochem. Res.* **23**(5), 583–587. https://doi.org/10.1023/a:1022470301550 (1998).
47. Resseguie, M. *et al.* Estrogen Regulation of the human PEMT (phosphatidylethanolamine N-methyltransferase) gene. *FASEB J.* **20**, A612–A612. https://doi.org/10.1096/fasebj.20.4.A612-c (2006).
48. Resseguie, M. E., Niculescu, M., Costa, K.-A.D., Randall, T. & Zeisel, S. Estrogen induces the PEMT (phosphatidylethanolamine N-methyltransferase) gene in human and murine hepatocytes. *FASEB J.* **21**, A61–A62. https://doi.org/10.1096/fasebj.21.5.A61-d (2007).
49. Noga, A. A. & Vance, D. E. A gender-specific role for phosphatidylethanolamine N-methyltransferase-derived phosphatidylcholine in the regulation of plasma high density and very low density lipoproteins in mice. *J. Biol. Chem.* **278**(24), 21851–21859. https://doi.org/10.1074/jbc.M301982200 (2003).
50. Gutiérrez-Juárez, R. *et al.* Critical role of stearoyl-CoA desaturase–1 (SCD1) in the onset of diet-induced hepatic insulin resistance. *J. Clin. Investig.* **116**(6), 1686–1695. https://doi.org/10.1172/JCI26991 (2006).
51. Yamaguchi, A., Botta, E. & Holinstat, M. Eicosanoids in inflammation in the blood and the vessel. *Front. Pharmacol.* **13**, 997403. https://doi.org/10.3389/fphar.2022.997403 (2022).
52. Chalfant, C. E. & Spiegel, S. Sphingosine 1-phosphate and ceramide 1-phosphate: Expanding roles in cell signaling. *J. Cell Sci.* **118**(20), 4605–4612. https://doi.org/10.1242/jcs.02637 (2005).
53. Han, M. S. *et al.* Lysophosphatidylcholine as an effector of fatty acid-induced insulin resistance. *J. Lipid Res.* **52**(6), 1234–1246. https://doi.org/10.1194/jlr.M014787 (2011).
54. Butler, M. G. Imprinting disorders in humans: A review. *Curr. Opin. Pediatr.* **32**, 719. https://doi.org/10.1097/MOP.0000000000000965 (2020).
55. May, J. C. *et al.* Conformational ordering of biomolecules in the gas phase: Nitrogen collision cross sections measured on a prototype high resolution drift tube ion mobility-mass spectrometer. *Anal. Chem.* **86**(4), 2107–2116. https://doi.org/10.1021/ac4038448 (2014).
56. Rose, B. S. *et al.* Improving confidence in lipidomic annotations by incorporating empirical ion mobility regression analysis and chemical class prediction. *Bioinformatics* **38**(10), 2872–2879. https://doi.org/10.1093/bioinformatics/btac197 (2022).
57. Hinz, C. *et al.* A comprehensive UHPLC ion mobility quadrupole time-of-flight method for profiling and quantification of eicosanoids, other oxylipins, and fatty acids. *Anal. Chem.* **91**(13), 8025–8035 (2019).
58. Poland, J. C. *et al.* Collision cross section conformational analyses of bile acids via ion mobility-mass spectrometry. *J. Am. Soc. Mass Spectrom.* **31**, 1625–1631 (2020).
59. Kanehisa, M. & Goto, S. KEGG: Kyoto encyclopedia of genes and genomes. *Nucleic Acids Res.* **28**(1), 27–30. https://doi.org/10.1093/nar/28.1.27 (2000).
60. Kanehisa, M. Toward understanding the origin and evolution of cellular organisms. *Protein Sci.* **28**, 1947–1951. https://doi.org/10.1002/pro.3715 (2019).
61. Kanehisa, M., Furumichi, M., Sato, Y., Kawashima, M. & Ishiguro-Watanabe, M. KEGG for taxonomy-based analysis of pathways and genomes. *Nucleic Acids Res.* **51**(D1), D587–D592. https://doi.org/10.1093/nar/gkac963 (2023).
62. Folch, J., Lees, M. & Sloanestanley, G. H. A simple method for the isolation and purification of total lipides from animal tissues. *J. Biol. Chem.* **226**(1), 497–509. https://doi.org/10.1016/s0021-9258(18)64849-5 (1957).
63. Morrison, W. R. & Smith, L. M. Preparation of fatty acid methyl esters and dimethylacetals from lipids with boron fluoride–methanol. *J. Lipid Res.* **5**(4), 600–608. https://doi.org/10.1016/s0022-2275(20)40190-7 (1964).
64. Sud, M. *et al.* Metabolomics Workbench: An international repository for metabolomics data and metadata, metabolite standards, protocols, tutorials and training, and analysis tools. *Nucleic Acids Res.* **44**(D1), D463–D470. https://doi.org/10.1093/nar/gkv1042 (2016).

65. Zhang, B. B., Zhou, G. & Li, C. AMPK: An emerging drug target for diabetes and the metabolic syndrome. *Cell Metab.* **9**(5), 407–416. https://doi.org/10.1016/j.cmet.2009.03.012 (2009).

Acknowledgements
The authors thank the Vanderbilt Genome Editing Resource for creating the *Atp10A* mouse lines and assisting with genotyping (supported by the Cancer Center Support Grant (CA68485), the Vanderbilt Diabetes Research and Training Center (DK020593) and the Center for Stem Cell Biology), the Vanderbilt Division of Animal Care veterinarians and technicians for their support with mouse husbandry, the Vanderbilt Metabolic Mouse Phenotyping Center (MMPC) especially Louise Lantier, for providing the NMR machine for body composition measurements and for performing the indirect calorimetry (DK135073, DK020593, S10RR028101), the Vanderbilt Analytical services core for measuring plasma and liver lipids (supported by *NIH grant DK020593 (DRTC))*, the Translational Pathology Shared Resource (TPSR) for producing all of the paraffin embedded tissue sections and performing the Oil Red O and CD31 staining (supported by NCI/NIH Cancer Center Support Grant P30CA068485), the Vanderbilt Cell Imaging Shared Resource (CISR) for providing the Zeiss LSM880 Airyscan Confocal Microscope used in this study (supported *by NIH grants CA68485, DK20593, DK58404, DK5 9637, and EY08126;* Zeiss LSM880 Airyscan Confocal Microscope *acquired through NIH* 1 S10 OD021630 1), the Center for Innovative Technology at Vanderbilt for providing access to the mass spectrometry instrumentation and lipidomics software, The Metabolomics Workbench *(supported by NIH grants U2C-DK119886 and OT2-OD030544),* Sophia Yu, Teri Stevenson, and Staci Bordash for help with mouse experiments, and Bridget Litts for help with finding materials and using equipment. We also thank David Wasserman, Owen McGuiness and David Harrison for helpful discussions. This work was supported by NIH 1R35GM144123 (to TRG), K01AG077038 (to LZ), NIH R01DK109102, R01HL144846, and T35DK7383, The Department of Veterans Affairs BX002223 (to JMS).

Author contributions
A.C.N. is the first author on this publication; she designed and conducted all of the mouse experiments, collected the tissues analyzed in the paper, and did the microscopy work. Additionally, she created the figures and schematics and wrote the manuscript. E.M.Y. conducted all of the western blot experiments, helped create the manuscript figures, and edited the manuscript. L.Z. helped with the mouse work, tissue collection, and provided intellectual support. BSR conducted the mass spectrometry analysis and analyzed the results. JCM developed the multidimensional mass spectrometry methods and assisted with the lipidomics informatics work. K.G.C. created the Oil Red O scoring system. J.A.M., J.M.S. and T.R.G. provided funding acquisition, resources, conceptualization, and project administration.

Competing interests
The authors declare no competing interests.

Additional information
Supplementary Information The online version contains supplementary material available at https://doi.org/10.1038/s41598-023-50360-5.

Correspondence and requests for materials should be addressed to T.R.G.